Chemically tuned p- and n-type WSe_2 monolayers with high carrier mobility for advanced electronics

Hyun Goo Ji, *Pablo Solís-Fernández*, *Daisuke Yoshimura, Mina Maruyama, Takahiko Endo*, *Yasumitsu Miyata*, *Susumu Okada*, *Hiroki Ago**

H. G. Ji, Prof. H. Ago
Interdisciplinary Graduate School of Engineering Sciences
Kyushu University
Fukuoka 816-8580, Japan
E-mail: h-ago@gic.kyushu-u.ac.jp

Dr. P. Solís-Fernández, Prof. H. Ago
Global Innovation Center (GIC)
Kyushu University
Fukuoka 816-8580, Japan

Dr. D. Yoshimura
Kyushu Synchrotron Light Research Center
Saga 841-0005, Japan

Dr. M. Maruyama, Prof. S. Okada
Graduate School of Pure and Applied Sciences
University of Tsukuba
Ibaraki 305-8571, Japan

T. Endo, Prof. Y. Miyata
Department of Physics
Tokyo Metropolitan University
Tokyo 192-0397, Japan

ABSTRACT

Monolayers of transition metal dichalcogenides (TMDCs) have attracted a great interest for post-silicon electronics and photonics due to their high carrier mobility, tunable band gap, and atom-thick two-dimensional structure. With the analogy to conventional silicon electronics, establishing a method to convert TMDC to p- and n-type semiconductors is essential for various device applications, such as complementary metal-oxide-semiconductor (CMOS) circuits and photovoltaics. Here, we demonstrate a successful control of the electrical polarity of monolayer WSe_2 by chemical doping. Two different molecules, nitrobenzenediazonium tetrafluoroborate (4-NBD) and diethylenetriamine (DETA), were utilized to convert ambipolar WSe_2 field-effect transistors (FETs) to p- and n-type, respectively. Moreover, the chemically doped WSe_2 showed increased effective carrier mobilities of 82 and 25 $cm^2V^{-1}s^{-1}$ for holes and electrons, respectively, which are much higher than those of the pristine WSe_2. The doping effects were studied by photoluminescence (PL), Raman, X-ray photoelectron spectroscopy (XPS), and density functional theory (DFT). Chemically tuned WSe_2 FETs were integrated into CMOS inverters, exhibiting extremely low power consumption (~0.17 nW). Furthermore, a p-n junction within single WSe_2 grain was realized via spatially-controlled chemical doping. Our chemical doping method for controlling the transport properties of WSe_2 will contribute to the development of TMDC-based advanced electronics.

Silicon forms the basis of the modern electronics, and controlled doping techniques have been widely used to fabricate both p- and n-type semiconductors made from silicon. Such spatially controlled doping techniques greatly contributed to the prevalence of Si-based complementary metal-oxide-semiconductor (CMOS) circuits, photovoltaic cells, and optical sensors. Atomically thin transition metal dichalcogenide (TMDC) semiconductors, a part of the family of two-dimensional (2D) materials, have attracted a great interest as a new alternative to silicon. This is because the monolayer TMDCs show excellent electrical transport properties with high on/off ratios, strong photoluminescence (PL) in the visible range, and tunable band gap ranging from 1.5 to 2 eV depending on the combination of transition metals and chalcogenides.[1–8] Recent development of the chemical vapor deposition (CVD) method for the wafer-scale growth of TMDCs have accelerated the research on their electronic and optoelectronic devices, including logic circuits, photodetectors, solar cells, and light emitting diodes.[7,9–13]

However, the precise control of the polarity in TMDC devices is still difficult, thus hindering practical applications. This is because most of TMDCs, such as MoS_2 and WS_2, are n-type semiconductors due to the unavoidable presence of S vacancies.[14,15] Attempts to convert n-type MoS_2 or WS_2 to p-type semiconductors have been reported. For example, partial substitution of Mo (or W) atoms with Nb and other metal atoms changed MoS_2 (or WS_2) to p-type character. However, the $Mo_xNb_{1-x}S_2$ devices show very weak gate dependence, reflecting a heavily degenerated state originated in the inserted Nb atoms.[16] Different types of dopants, such as thiol-based molecules and Zn atoms, were also used to dope MoS_2.[17,18] In these works, the threshold voltage (V_{th}) of devices shifts to higher gate voltages reflecting hole doping, but the main carriers are still electrons as observed from the corresponding transfer characteristics.[17,18]

Being different from MoS_2 and WS_2, pristine WSe_2 is known to show ambipolar behavior. Chen *et al.* reported the p-doping effect of Au nanoparticles deposited on WSe_2.[19]

However, the Au-coated WSe_2 still shows ambipolar behavior rather than p-type transport. Moreover, the PL from WSe_2 was strongly quenched by the nanoparticles, which is a disadvantage for optical applications. In ambient condition, p-type transport characteristics were observed for WSe_2.[20,21] Different metal contacts, Pd and Ag were used to operate p-type and n-type WSe_2, respectively,[22,23] though multiple electrode deposition processes are needed for the device fabrication. Partial substitution of Se atom with P was reported to induce p-type doping on WSe_2, but its influence on the electrical transport property was not studied.[24] In contrast, a mild plasma treatment was introduced to generate Se defect on WSe_2 to achieve n-type doping.[25] The defect engineering was utilized only for n-type doping but not for p-type doping and, more importantly, Se defects generally deteriorate the physical properties.

Consequently, it is difficult to obtain both p- and n-type transport properties using an identical TMDC without changing the contact metal. Therefore, previous works combined different types of TMDCs, such as p-type WSe_2 (or p-type $MoTe_2$) and n-type MoS_2, to fabricate CMOS circuits.[13,26,27] Alternatively, very high effective gate voltages were applied to operate p- and n-type WSe_2 channels with the aid of ionic liquid.[28] Recently molecular doping technique was applied to various exfoliated TMDC flakes, and both p- and n-type doping effects were observed. In this work, however, different metals, Pd and Ti, were used for p- and n-doping, and the use of exfoliated TMDC flakes limited the practical applications.[29]

In this Communication, we demonstrate the chemical doping of large-area CVD-grown WSe_2 monolayers for selective conversion from ambipolar to p- and n-type semiconductors without changing the contact electrodes. We found that the doping treatments increased the effective carrier mobilities up to four orders of magnitude above the threshold region with respect to the pristine WSe_2, obtaining maximum values of 82 $cm^2V^{-1}s^{-1}$ and 25 $cm^2V^{-1}s^{-1}$ for holes and electrons, respectively. The chemically doped WSe_2 monolayers were integrated

into CMOS circuits that showed extremely low power consumption (~ 170 pW with V_{gain} of ~10). Moreover, spatially controlled doping was also achieved within a single WSe_2 grain to obtain separated p- and n-doped regions. The WSe_2 grain with the artificial p-n junction showed clear rectification behavior and optical response to visible light, implying its potential for photodetection applications.[30–34]

Figure 1 shows the experimental procedure employed to prepare p- and n-doped WSe_2. Triangular grains of monolayer WSe_2 were synthesized on SiO_2/Si substrates by thermal CVD using WO_3 and Se precursors. An optical microscope image of the as-grown WSe_2 is shown in Figure 1b. To avoid gate leakage, the as-grown WSe_2 was transferred to a fresh SiO_2(90 nm)/Si substrate.[35] After the transfer, field-effect transistors (FETs) with WSe_2 channels were fabricated by photolithography, Ni/Au electrode deposition, and lift-off processes.

For the p-type doping, the WSe_2 was immersed in aqueous solution of 4-nitrobenzenediazonium tetrafluoroborate (4-NBD) (Figure 1c), while WSe_2 was exposed to diethylenetriamine (DETA) vapor for the n-type doping (Figure 1d). Atomic force microscope (AFM) images of pristine, 4-NBD and DETA doped WSe_2 grains are shown in Supporting information, Figure S1. The as-grown, pristine WSe_2 had a thickness of ~ 1 nm and showed an intense PL at 760 nm, reflecting the direct band gap nature. These results confirm the growth of monolayer WSe_2. Figure 1e shows the device structure of WSe_2-FET and the corresponding transfer characteristics measured before and after the chemical doping. Drain current (I_d) was measured as a function of gate voltage (V_g) applied from back side of the device through a SiO_2 layer. The pristine WSe_2 (black curve) showed ambipolar behavior with a slightly n-doped character. After the contact with 4-NBD and DETA dopants, the WSe_2 device changed to p- (red curve) and n-type (blue curve), respectively. The V_{th} shifted to more positive (p-doped) and more negative (n-doped) voltages after each doping. This implies that holes and electrons are accumulated not only by the gate voltage but also by the

chemical doping effect. The transfer curves with linear scale of the drain current are shown in Figure S2.

We note that the slopes of the transfer curve after the doping are much steeper than those of the undoped devices (see Figure 1e, in which *y*-axis scale is logarithmic). **Figure 2**a,b shows more detailed analysis of the carrier transport of the doped WSe_2 monolayers. To avoid device-to-device variations, we measured the electrical transport of the same WSe_2 channels before and after the doping process. Because the V_{th} are different for the pristine and doped WSe_2 samples, the overdrive gate voltage (V_g-V_{th}) was used in the graphs for better comparison of the gate voltage dependence. The effective field-effect carrier mobility (μ) was calculated by using the following equation:

$$\mu = \frac{g_m}{C_{ox} V_d} \frac{L}{W} \quad (1)$$

where $g_m = dI_d/dV_g$ is the transconductance obtained from the transfer curve; $C_{ox} = 38.3$ nFcm^{-2} is the capacitance per unit area of the 90 nm-thick SiO_2; V_d is the applied drain voltage; L and W represent the effective length and width of the channel. The effective carrier mobility was calculated by assuming a trapezoidal channel shape to take into account the geometrical effect. It is seen that the carrier mobility after the doping with both 4-NBD and DETA increased by more than 3-4 orders of magnitude.

Figure 2c compares the effective carrier mobilities of WSe_2 devices (20 devices were measured for each dopant). The measured hole and electron mobilities of the pristine WSe_2 were found to be rather low. This can originate in intrinsic defects in the as-grown WSe_2 grains, degradation due to air exposure, and/or possible damages induced by the device fabrication process, as based on our experience WSe_2 is easier to be oxidized than MoS_2 and WS_2. Interestingly, both the hole and electron mobilities drastically increased after the chemical doping, as can be seen in Figure 2c. The maximum carrier mobilities measured after the p- and n-type doping were 82 cm^2 V^{-1}s^{-1} (for holes) and 25 cm^2 V^{-1}s^{-1} (for electrons),

respectively. We speculate that influence of defects existing in WSe_2 is reduced by the chemical doping due to increased carrier concentration, contributing to the increase of the measured carrier mobilities. In addition, the lowering the Schottky barrier height due to the chemical doping-induced Fermi level shift should be considered as another source of the increased effective carrier mobility. In previous literatures,[23,36–39] it has been proposed that the interface between the 2D material and the electrode plays an important role in the carrier transport due to strong modification of the Fermi level of the 2D material. Thus, it is highly likely that reduction of the contact resistance induced by the chemical doping largely contributes to the increased carrier mobility of WSe_2 FETs. The enhanced carrier mobilities together with the polarity control would allow prospective use for high mobility switching devices.

Figures 3a and 3b compare the PL spectra of monolayer WSe_2 before and after the doping with 4-NBD and DETA, respectively. The 4-NBD doping was found to increase the PL intensity and decrease the full-width at half-maximum (FWHM) from 64 to 53 meV. The PL peak from the pristine WSe_2 can be deconvoluted with exciton and trion peaks located at ~1.64 eV and ~1.59 eV, respectively, as shown in Figure S3. As reported previously, it is considered that the trion in the pristine WSe_2 is a negative trion (A^-),[40] being consistent with the experimental observation that electrons are main charge carriers in the absence of a gate voltage (see Figure 1e). The 4-NBD doping increased the intensity of the exciton peak while reduced that of the trion (Figures 3a and S2). The increased exciton peak can be accounted for by the reduction of the negative charges due to the supply of holes from 4-NBD, resulting in the decreased ratio of negative trions. The trion peak in the doped WSe_2 can be either remaining negative trions or newly formed positive trions. Although the origin of the trion peak is unclear, the PL spectra supports the hole doping to the WSe_2 induced by 4-NBD molecules.

The DETA doping gave a completely different change in the PL spectrum (Figure 3b). The PL peak was strongly suppressed and red-shifted by ~50 meV. The fitting analysis indicates that the spectral weight of the trion peak increased, while the exciton peak decreased significantly (see Figure S3). This can be explained by the increased concentration of negative trions, while preventing the formation of neutral excitons as a result of electron doping.[29,41] In this case, the observed trion peak should be originated in the negative trions. The observed peak shift of ~50 meV after the DETA doping corresponds to the trion binding energy of WSe_2.[42,43]

Effects of the chemical doping on the Raman spectrum were also studied, as shown in Fig. 3c. The E^1_{2g} band which corresponds to the in-plane vibration mode clearly shifted to higher and lower wavenumbers upon 4-NBD and DETA doping, respectively. The position of the out-of-plane mode (A_{1g} band) exhibited a similar tendency. Such doping-induced Raman shift is consistent with previous studies,[44,45] and can be explained by the change of the electron density in monolayer WSe_2; the n-type doping increases the electron-phonon scattering due to a higher electron concentration, while the p-type doping decreases the electron-phonon scattering.[44,45] The decrease of the A_{1g} peak intensity is also in accordance with the existing literature.[19,44] Thus, the Raman spectroscopy also supports the p/n selective doping in our CVD-grown WSe_2.

For further understanding of the changes of the WSe_2 electronic structure induced by 4-NBD and DETA molecules as well as the charge transfer phenomena, X-ray photoelectron spectroscopy (XPS) measurement and density functional theory (DFT) calculations were performed. **Figure 4**a,b shows XPS W_{4f} and Se_{3d} spectra of the pristine and the doped WSe_2. The chemical doping with 4-NBD molecule shifted the binding energies of both W_{4f} and Se_{3d} peaks to lower energies (see Table S1 for the XPS peak positions). This shift implies that the Fermi level of the WSe_2 is moved downward to the valence band edge. On the other hand, the DETA doping increased the binding energies of both W_{4f} and Se_{3d} peaks, suggesting the

shifting of the Fermi energy upward to the conduction band edge. These observed energy shifts are consistent with the previous literatures reporting the selective p/n-doping to MoS_2.[29,46,47] Therefore, the changes of the binding energies after the 4-NBD and DETA adsorption qualitatively supports the p-/n-selective doping by tuning the Fermi energy of the monolayer WSe_2.

Figures 4c and S4 display the energy levels of WSe_2, 4-NBD, and DETA, as determined by the DFT calculations. In the case of 4-NBD, the diazonium molecule forms a complex with BF_4^- anion.[48] Therefore, in the present calculation, the diazonium molecule is assumed to possess a singly occupied molecular orbital (SOMO) located between the highest occupied molecular orbital (HOMO) and the lowest unoccupied molecular orbital (LUMO). As seen in Figure 4c, the relative position of SOMO of 4-NBD and valence band edge (VBE) of WSe_2 supports the hole doping in WSe_2 via the electrons transfer to the SOMO.

DETA molecule has a closed-shell electronic structure and its HOMO locates within the band gap of pristine, monolayer WSe_2 (see Figure S4 for the band energy of the pristine WSe_2). However, the HOMO level is ~1.59 eV below the conduction band edge (CBE) of WSe_2 (Figure S4). We think that there are several mechanisms that assist the electron transfer from DETA to WSe_2. First, Se vacancies are frequently observed in WSe_2 samples,[49] which can be the origin of the relatively low effective carrier mobility observed in our pristine WSe_2 (see Figure 2c). Therefore, in Figure 4c, we show the band structure of the monolayer WSe_2 containing Se vacancies (one Se atom was removed from 4×4 unit cell, which corresponds to ~3% Se vacancy (see Figure S5 for the atomic structure)). As seen in Figure 4c, the introduction of Se vacancies produced a new state, which is associated with the defect, at 0.61 eV below the CBE. This defect state is expected to act as an intermediate trap state through which the electrons transfer from DETA to WSe_2, thus assisting the n-type doping. Although we do not know the exact density of structural defects including Se vacancies, the post-growth treatment, such as exposure to ambient and the device fabrication process, may give more

defects and with more variety of defect structures. It is noted that a scanning transmission electron microscope (STEM) study revealed the presence of various crystal defects in monolayer MoS_2, suggesting the formation of localized electronic states within the bandgap.[50] Other DFT calculations also indicated the formation of a defect state (or in-gap state) within the band gap when chalcogen vacancies are introduced in MoS_2 and $MoSe_2$.[51,52] Therefore, we think that there is a possibility that the defect-related bands appear just above the HOMO level of DETA or close to the HOMO level, which can account for the experimentally observed n-type doping. The second possibility is the coordination of paired electrons of N atoms in DETA to W atoms of WSe_2, introducing the charge transfer to WSe_2. As this model is also based on the presence of Se vacancies to access a W metal, we speculate that the imperfect WSe_2 structure is related to the observed n-type doping induced by DETA molecules.

To support our interpretation of the doping mechanism in WSe_2, we also treated monolayer WS_2 with 4-NBD and DETA for the sake of comparison. The PL spectral change is presented in Supporting Information, Figure S6. A similar tendency was observed for monolayer WS_2, with an increased ratio of the exciton peak after 4-NBD doping, and the significant increase of the trion peak after DETA doping.[53,54] As shown in Figure S7a, the WS_2 FET showed the shift of V_{th} to positive gate voltages after dipping in 4-NBD solution, but it did not show p-type transport character. According to DFT calculations (see Figure S4), the VBE of WS_2 is located below the SOMO of 4-NBD, making it difficult to inject holes from 4-NBD to WS_2. This is consistent with the FET result in which clear p-type transfer characteristics was not observed in 4-NBD doped WS_2 system (see Figure S7a). The exposure to DETA vapor shifted the V_{th} of WS_2 to negative voltages, indicating the n-type doping (Figure S7b). This agrees with the calculated band structure, as the defect state of WS_2 is closer to the HOMO level of DETA than the defect state of WSe_2 (see Figure S4).

Our experimental and theoretical results indicate that monolayer WSe_2 is suitable for obtaining clear p/n selective doping with the employed dopant molecules.

Previously, formation of a covalent bond was proposed between a 4-NBD molecule and monolayer TMDC,[55,56] similar to the case of graphene and 4-NBD.[48] In the case of graphene, the covalent bond formation can be recognized from the appearance of defect-related Raman D-band. However, as the Raman spectrum of TMDCs is not so sensitive to defects or covalent bond formation, it is difficult to experimentally discuss how the dopant molecules attach on the WSe_2. The p-doping effect in the 4-NBD doped WSe_2 was still observed after thorough washing with water, while n-type doping effect by DETA disappeared easily after washing with water. Thus, there is a possibility of chemisorption and physisorption for 4-NBD and DETA doping, respectively. However, the XPS spectra of 4-NBD doped WSe_2 (Figure 4a,b) did not show any apparent changes in the peak shapes except for shift of the peak positions to lower binding energies. There is no solid evidence for the possible chemisorption of 4-NBD molecules on WSe_2 surface. Therefore, further study is necessary to understand the detailed doping mechanism by employing atomic scale imaging techniques, such as transmission electron microscope (TEM) and scanning tunneling microscope (STM).

The controlled p- and n-type doping in WSe_2 was developed to fabricate a CMOS inverter. **Figure 5**a shows the input voltage (V_{in}) dependence of the output voltage (V_{out}) collected with different supply voltages (V_d). Here, the p- and n-FETs were externally connected in series by an Au wire to form the inverter, with the common back-gate being the input (V_{in}) (See Figure 5a inset). As can be seen in Figure 5a, the V_{in} signal was properly inverted. The V_{out} was kept at a value of V_d for V_{in} lower than ~ -28 V and dropped to ~0 V for V_{in} higher than ~-25 V, with a sharp inversion. Figure 5b shows the voltage gain, defined as $V_{gain} = -dV_{out}/dV_{in}$, which is one of the most important performance parameters of CMOS inverters. As can be expected from the sharp transition of V_{out} (Figure 5a), a maximum V_{gain}

as high as 10 was achieved. To the best of our knowledge, this is the first report of a CVD-grown WSe_2 CMOS inverter where both p- and n-channels are formed by respective doping treatments.[13,26,57–61] Considering that this CMOS circuit was fabricated on a SiO_2 (90 nm)/Si substrate with a back-gate geometry (C_{ox} = 38.3 nF cm^{-2}), the obtained gain can be further improved by increasing the capacitance via a top-gate operation for a more effective switching control.[13,23]

One of the biggest benefits of CMOS circuits is their low power operation. Figure 5c shows the power consumption of the WSe_2-based inverter as a function of the input voltage. We found that our inverter can be operated with an extremely low power consumption of ~170 pW. This value is three orders of magnitude lower than those from previous references using TMDC channels.[13,26,57] We attribute this low power consumption to the optimized overlap of the transfer curves of p- and n-FETs, allowing to keep the current flow through the inverter low. As shown in Figure S8, the power consumption of our inverters increased with increasing the overlap of the transfer curves of p- and n-FETs. Liu *et al*. reported 1 μW power consumptions when the transfer curves of the individual FETs overlap at a drain current of ~1000 nA.[60] Zhang *et al.* reported 3.1 nW power consumptions when the overlap of the individual FETs transfer curves occurs at 1 nA.[57] In contrast, our p- and n-FETs overlapped at ~0.1 nA, thus efficiently minimizing the leakage current to prevent the power loss. Therefore, controlled doping through the optimization of the exposure time and dopant concentration is required for both p- and n-type WSe_2 to achieve low power CMOS inverters.

For practical applications of TMDC materials in electronic and optoelectronic devices, the p-n junction is the most important and basic working unit. Therefore, we fabricated a p-n junction within a single WSe_2 grain through spatially controlled p- and n-doping. The fabrication process is depicted in Figure S9. In brief, 4-NBD doping was performed through a photoresist window, followed by deposition of SiO_2 as a protective layer. Then, another window is opened in the SiO_2 layer for the successive DETA doping. **Figures 6**a and 6b

show a false colored optical image and the corresponding schematic model of the p-n doped single grain device fabricated in this work. Output characteristics of the WSe_2 before and after the formation of the p-n junction are shown in Figure 6c. While the pristine WSe_2 grain exhibited an almost linear I_d-V_d curve with high resistivity (black curve), after the spatially controlled p-n doping, the device showed a clear rectifying behavior (red curve). Such asymmetric transport behavior is a strong evidence for the formation of a p-n junction.[30,31,62] Under illumination with visible light (532 nm, 6.4 $mWcm^{-2}$), we observed a clear photoresponse (Figure 6d), demonstrating its potential in photodetection applications.

In conclusion, we have demonstrated the effective and controlled chemical doping of CVD-grown WSe_2. Spectroscopic analyses and DFT calculation proved that 4-NBD and DETA molecules allow efficient charge transfer to WSe_2, changing the ambipolar WSe_2 to p- and n-type semiconductors, respectively. The chemical doping with 4-NBD and DETA was found to significantly improve the effective carrier mobilities of both holes and electrons. We have also demonstrated the integration of the p- and n-type WSe_2 for the operation of a low power CMOS inverter, owing to the high control of the degree of the doping. Moreover, the position selective doping has been developed to obtain the p-n junction within a single WSe_2 grain. The p-n doped WSe_2 grain showed clear rectification behavior and optical response, as required for optoelectronics applications. We believe that our chemical doping strategy offer a versatile approach to modify the electrical property of TMDC materials for various device applications.

Experimental Section

CVD growth of WSe_2 and WS_2: Monolayer WSe_2 was synthesize by an improved salt-assisted CVD method using WO_3 powder and Se beads. We also used KBr powder which acts act as a growth promoter.[22] In a tubular furnace, WO_3 and KBr were placed 2 cm and 9 cm upstream of the SiO_2/Si substrate. Temperatures of the substrate and the WO_3 were gradually increased to the growth temperature (780 °C) with a N_2/H_2 gas mixture at a flow rate of 400/1.2 ccm. After the substrate reached the growth temperature, Se was heated to 300~370 °C by using another furnace to supply Se vapor to grow WSe_2. After 10 min reaction, the sample was cooled down immediately.

WS_2 was synthesized by ambient pressure CVD method using WO_3 powder and S power. No growth promoter was used for the WS_2 growth, but we used c-plane sapphire as a growth substrate. The details of the WS_2 synthesis are reported elsewhere.[32]

Chemical doping: For p-type doping, a WSe_2 sample was immersed in aqueous solution of 4-NBD with concentrations of 10~100 mM and left in dark environment. The sample was kept in the solution at 60 °C for 30 minutes. For n-type doping, a WSe_2 sample was exposed to DETA vapor (~460 Pa vapor pressure) at 70 °C for 30 minutes.[63] In the closed petri dish with ~100 cm^3 volume, 300 μL of DETA was placed for applying DETA vapor to WSe_2.

Characterizations: Optical micrographs were taken using an optical microscope (Nikon Eclipse ME 600), and the AFM height images were collected using a Nanoscope V Multimode SPM (Bruker Co.). PL and Raman spectra were measured using a confocal Raman spectroscope (Tokyo Instruments Inc., Nanofinder 30) under 532 nm laser excitation. XPS measurements were conducted in the beamline 10 (BL10) of SAGA Light Source (SAGA-LS) at 10^{-8} Pa with the incident energy of 600 eV. For the XPS measurement, WSe_2 grains were transferred to an Au-coated SiO_2/Si substrate, followed by respective doping processes.

DFT calculation: Electronic structure calculations of DETA, 4-NBD, and WSe_2 were conducted using the DFT implemented in the STATE code.[64] The exchange correlation interaction among interacting electrons is expressed by the generalized gradient approximation (GGA) with the PBE functional form. For the electron-ion interaction, we adopted ultrasoft pseudopotentials generated by the Vanderbilt scheme. The valence wave functions and deficit charge density were expanded in conjunction with a plane-wave basis set, applying cutoff energies of 25 and 225 Ryd, respectively. To obtain qualitative insight into the possibility of the charge transfer from the dopant molecules, 4NBD and DETA, to WSe_2, we evaluated the absolute values of the electron energy levels of isolated 4-NBD, DETA, and WSe_2 by DFT calculations. For the evaluation of the energy level with respect to the vacuum, we conducted super cell calculations for isolated molecules and WSe_2 in which the molecules or WSe_2 are separated their periodic images by at least 1.5 nm vacuum spacing. For WSe_2, we consider a 4×4 lateral periodicity to evaluate the effect of chalcogen defects on the electronic energy band. The geometric structures were optimized until the remaining force acting on the atoms becomes smaller than 0.005 Ryd/Å.

Device fabrication and measurement: As the CVD process slightly damaged the surface SiO_2 layer and gave gate leakage, we transferred the as-grown WSe_2 grains onto a fresh SiO_2(90 nm)/Si substrate using polystyrene as a support layer.[35] Prior to the transfer, the SiO_2 /Si substrates were cleaned by sonicating in acetone and isopropyl alcohol for 10 minutes each. For the fabrication of FETs, the transferred WSe_2 was spin-coated by photoresist and patterned using photolithography, followed by electron beam evaporation of Au(30 nm)/Ni(1 nm) electrodes (Kennix KB-750) and lift-off process. Carrier transport properties were measured using a semiconductor parameter analyzer (Keysight Technologies B1500A) in vacuum (~10^{-4} Pa) at room temperature. To fabricate the inverter circuit, two WSe_2 FETs were externally connected by Au wire (99.95 %, 300 μm in diameter). The inverter performance was also measured in a vacuum (~10^{-4} Pa) at room temperature. For measuring

the optical response of a p-n device, a 532 nm laser (Showa Optronics Co.) was used together with ND filters for controlling the laser power.

Supporting Information
Supporting Information is available from the Wiley Online Library or from the author.

Acknowledgements
This work was supported by JSPS KAKENHI grant numbers JP17K19036, JP18H01832, and JP18H03864 and JST CREST grant numbers JPMJCR18I1 and JPMJCR16F3.

Keyword
tungsten diselenide, chemical vapor deposition, chemical doping, complementary inverter, p-n junction

Received: ((will be filled in by the editorial staff))
Revised: ((will be filled in by the editorial staff))
Published online: ((will be filled in by the editorial staff))

References

[1] Z. Y. Zhu, Y. C. Cheng, U. Schwingenschlögl, *Phys. Rev. B* **2011**, *84*, 153402.
[2] Q. H. Wang, K. Kalantar-Zadeh, A. Kis, J. N. Coleman, M. S. Strano, *Nat. Nanotechnol.* **2012**, *7*, 699.
[3] T. Cheiwchanchamnangij, W. R. L. Lambrecht, *Phys. Rev. B* **2012**, *85*, 205302.
[4] K. Kang, S. Xie, L. Huang, Y. Han, P. Y. Huang, K. F. Mak, C.-J. Kim, D. Muller, J. Park, *Nature* **2015**, *520*, 656.
[5] K. M. McCreary, A. T. Hanbicki, G. G. Jernigan, J. C. Culbertson, B. T. Jonker, *Sci. Rep.* **2016**, *6*, 19159.
[6] K. K. H. Smithe, S. V. Suryavanshi, M. Muñoz Rojo, A. D. Tedjarati, E. Pop, *ACS Nano* **2017**, *11*, 8456.
[7] A. S. Aji, P. Solís-Fernández, H. G. Ji, K. Fukuda, H. Ago, *Adv. Funct. Mater.* **2017**, *27*, 1703448.
[8] H. Kim, G. H. Ahn, J. Cho, M. Amani, J. P. Mastandrea, C. K. Groschner, D.-H. Lien, Y. Zhao, J. W. Ager, M. C. Scott, D. C. Chrzan, A. Javey, *Sci. Adv.* **2019**, *5*, eaau4728.
[9] D. Jariwala, V. K. Sangwan, L. J. Lauhon, T. J. Marks, M. C. Hersam, *ACS Nano* **2014**, *8*, 1102.
[10] M.-L. Tsai, S.-H. Su, J.-K. Chang, D.-S. Tsai, C.-H. Chen, C.-I. Wu, L.-J. Li, L.-J. Chen, J.-H. He, *ACS Nano* **2014**, *8*, 8317.
[11] W. Yang, J. Shang, J. Wang, X. Shen, B. Cao, N. Peimyoo, C. Zou, Y. Chen, Y. Wang, C. Cong, W. Huang, T. Yu, *Nano Lett.* **2016**, *16*, 1560.
[12] S. Wachter, D. K. Polyushkin, O. Bethge, T. Mueller, *Nat. Commun.* **2017**, *8*, 14948.
[13] J. Pu, K. Funahashi, C.-H. Chen, M.-Y. Li, L.-J. Li, T. Takenobu, *Adv. Mater.* **2016**, *28*, 4111.
[14] V. Carozo, Y. Wang, K. Fujisawa, B. R. Carvalho, A. McCreary, S. Feng, Z. Lin, C. Zhou, N. Perea-López, A. L. Elías, B. Kabius, V. H. Crespi, M. Terrones, *Sci. Adv.* **2017**, *3*, e1602813.
[15] H. G. Ji, Y.-C. Lin, K. Nagashio, M. Maruyama, P. Solís-Fernández, A. Sukma Aji, V. Panchal, S. Okada, K. Suenaga, H. Ago, *Chem. Mater.* **2018**, *30*, 403.
[16] J. Suh, T.-E. Park, D.-Y. Lin, D. Fu, J. Park, H. J. Jung, Y. Chen, C. Ko, C. Jang, Y. Sun, R. Sinclair, J. Chang, S. Tongay, J. Wu, *Nano Lett.* **2014**, *14*, 6976.
[17] D. M. Sim, M. Kim, S. Yim, M.-J. Choi, J. Choi, S. Yoo, Y. S. Jung, *ACS Nano* **2015**, *9*, 12115.
[18] E. Z. Xu, H. M. Liu, K. Park, Z. Li, Y. Losovyj, M. Starr, M. Werbianskyj, H. A. Fertig, S. X. Zhang, *Nanoscale* **2017**, *9*, 3576.
[19] C.-H. Chen, C.-L. Wu, J. Pu, M.-H. Chiu, P. Kumar, T. Takenobu, L.-J. Li, *2D Mater.* **2014**, *1*, 034001.
[20] H. Zhou, C. Wang, J. C. Shaw, R. Cheng, Y. Chen, X. Huang, Y. Liu, N. O. Weiss, Z. Lin, Y. Huang, X. Duan, *Nano Lett.* **2015**, *15*, 709.
[21] Y. Gao, Y.-L. Hong, L.-C. Yin, Z. Wu, Z. Yang, M.-L. Chen, Z. Liu, T. Ma, D.-M. Sun, Z. Ni, X.-L. Ma, H.-M. Cheng, W. Ren, *Adv. Mater.* **2017**, *29*, 1700990.
[22] S. Li, S. Wang, D.-M. Tang, W. Zhao, H. Xu, L. Chu, Y. Bando, D. Golberg, G. Eda, *Appl. Mater. Today* **2015**, *1*, 60.
[23] H. Fang, S. Chuang, T. C. Chang, K. Takei, T. Takahashi, A. Javey, *Nano Lett.* **2012**, *12*, 3788.
[24] W. T. Kang, I. M. Lee, S. J. Yun, Y. I. Song, K. Kim, D.-H. Kim, Y. S. Shin, K. Lee, J. Heo, Y.-M. Kim, Y. H. Lee, W. J. Yu, *Nanoscale* **2018**, *10*, 11397.
[25] M. Tosun, L. Chan, M. Amani, T. Roy, G. H. Ahn, P. Taheri, C. Carraro, J. W. Ager, R. Maboudian, A. Javey, *ACS Nano* **2016**, *10*, 6853.

[26] P. J. Jeon, J. S. Kim, J. Y. Lim, Y. Cho, A. Pezeshki, H. S. Lee, S. Yu, S.-W. Min, S. Im, *ACS Appl. Mater. Interfaces* **2015**, *7*, 22333.
[27] Y. Cho, J. H. Park, M. Kim, Y. Jeong, S. Yu, J. Y. Lim, Y. Yi, S. Im, *Nano Lett.* **2019**, *19*, 2456.
[28] J.-K. Huang, J. Pu, C.-L. Hsu, M.-H. Chiu, Z.-Y. Juang, Y.-H. Chang, W.-H. Chang, Y. Iwasa, T. Takenobu, L.-J. Li, *ACS Nano* **2014**, *8*, 923.
[29] S. Zhang, H. M. Hill, K. Moudgil, C. A. Richter, A. R. H. Walker, S. Barlow, S. R. Marder, C. A. Hacker, S. J. Pookpanratana, *Adv. Mater.* **2018**, *30*, 1806345.
[30] C.-H. Lee, G.-H. Lee, A. M. van der Zande, W. Chen, Y. Li, M. Han, X. Cui, G. Arefe, C. Nuckolls, T. F. Heinz, J. Guo, J. Hone, P. Kim, *Nat. Nanotechnol.* **2014**, *9*, 676.
[31] M.-Y. Li, Y. Shi, C.-C. Cheng, L.-S. Lu, Y.-C. Lin, H.-L. Tang, M.-L. Tsai, C.-W. Chu, K.-H. Wei, J.-H. He, W.-H. Chang, K. Suenaga, L.-J. Li, *Science* **2015**, *349*, 524.
[32] A. S. Aji, M. Izumoto, K. Suenaga, K. Yamamoto, H. Nakashima, H. Ago, *Phys. Chem. Chem. Phys.* **2018**, *20*, 889.
[33] A. Henning, V. K. Sangwan, H. Bergeron, I. Balla, Z. Sun, M. C. Hersam, L. J. Lauhon, *ACS Appl. Mater. Interfaces* **2018**, *10*, 16760.
[34] D. Tan, X. Wang, W. Zhang, H. E. Lim, K. Shinokita, Y. Miyauchi, M. Maruyama, S. Okada, K. Matsuda, *Small* **2018**, *14*, 1704559.
[35] A. Gurarslan, Y. Yu, L. Su, Y. Yu, F. Suarez, S. Yao, Y. Zhu, M. Ozturk, Y. Zhang, L. Cao, *ACS Nano* **2014**, *8*, 11522.
[36] X. Liu, D. Qu, J. Ryu, F. Ahmed, Z. Yang, D. Lee, W. J. Yoo, *Adv. Mater.* **2016**, *28*, 2345.
[37] S. McDonnell, R. Addou, C. Buie, R. M. Wallace, C. L. Hinkle, *ACS Nano* **2014**, *8*, 2880.
[38] M.-Y. Tsai, S. Zhang, P. M. Campbell, R. R. Dasari, X. Ba, A. Tarasov, S. Graham, S. Barlow, S. R. Marder, E. M. Vogel, *Chem. Mater.* **2017**, *29*, 7296.
[39] H.-J. Chuang, X. Tan, N. J. Ghimire, M. M. Perera, B. Chamlagain, M. M.-C. Cheng, J. Yan, D. Mandrus, D. Tománek, Z. Zhou, *Nano Lett.* **2014**, *14*, 3594.
[40] Z. Li, T. Wang, Z. Lu, C. Jin, Y. Chen, Y. Meng, Z. Lian, T. Taniguchi, K. Watanabe, S. Zhang, D. Smirnov, S.-F. Shi, *Nat. Commun.* **2018**, *9*, 3719.
[41] Z. Wu, W. Zhao, J. Jiang, T. Zheng, Y. You, J. Lu, Z. Ni, *J. Phys. Chem. C* **2017**, *121*, 12294.
[42] A. M. Jones, H. Yu, N. J. Ghimire, S. Wu, G. Aivazian, J. S. Ross, B. Zhao, J. Yan, D. G. Mandrus, D. Xiao, W. Yao, X. Xu, *Nat. Nanotechnol.* **2013**, *8*, 634.
[43] J.-W. Chen, S.-T. Lo, S.-C. Ho, S.-S. Wong, T.-H.-Y. Vu, X.-Q. Zhang, Y.-D. Liu, Y.-Y. Chiou, Y.-X. Chen, J.-C. Yang, Y.-C. Chen, Y.-H. Chu, Y.-H. Lee, C.-J. Chung, T.-M. Chen, C.-H. Chen, C.-L. Wu, *Nat. Commun.* **2018**, *9*, 3143.
[44] Y. Shi, J.-K. Huang, L. Jin, Y.-T. Hsu, S. F. Yu, L.-J. Li, H. Y. Yang, *Sci. Rep.* **2013**, *3*, 1839.
[45] P. T. K. Loan, W. Zhang, C.-T. Lin, K.-H. Wei, L.-J. Li, C.-H. Chen, *Adv. Mater.* **2014**, *26*, 4838.
[46] A. Tarasov, S. Zhang, M.-Y. Tsai, P. M. Campbell, S. Graham, S. Barlow, S. R. Marder, E. M. Vogel, *Adv. Mater.* **2015**, *27*, 1175.
[47] J. D. Lin, C. Han, F. Wang, R. Wang, D. Xiang, S. Qin, X.-A. Zhang, L. Wang, H. Zhang, A. T. S. Wee, W. Chen, *ACS Nano* **2014**, *8*, 5323.
[48] M. A. Bissett, S. Konabe, S. Okada, M. Tsuji, H. Ago, *ACS Nano* **2013**, *7*, 10335.
[49] Y.-C. Lin, T. Björkman, H.-P. Komsa, P.-Y. Teng, C.-H. Yeh, F.-S. Huang, K.-H. Lin, J. Jadczak, Y.-S. Huang, P.-W. Chiu, A. V. Krasheninnikov, K. Suenaga, *Nat. Commun.* **2015**, *6*, 6736.
[50] W. Zhou, X. Zou, S. Najmaei, Z. Liu, Y. Shi, J. Kong, J. Lou, P. M. Ajayan, B. I. Yakobson, J.-C. Idrobo, *Nano Lett.* **2013**, *13*, 2615.

[51] S. Barja, S. Refaely-Abramson, B. Schuler, D. Y. Qiu, A. Pulkin, S. Wickenburg, H. Ryu, M. M. Ugeda, C. Kastl, C. Chen, C. Hwang, A. Schwartzberg, S. Aloni, S.-K. Mo, D. Frank Ogletree, M. F. Crommie, O. V. Yazyev, S. G. Louie, J. B. Neaton, A. Weber-Bargioni, *Nat. Commun.* **2019**, *10*, 3382.
[52] H. Qiu, T. Xu, Z. Wang, W. Ren, H. Nan, Z. Ni, Q. Chen, S. Yuan, F. Miao, F. Song, G. Long, Y. Shi, L. Sun, J. Wang, X. Wang, *Nat. Commun.* **2013**, *4*, 2642.
[53] M. Okada, Y. Miyauchi, K. Matsuda, T. Taniguchi, K. Watanabe, H. Shinohara, R. Kitaura, *Sci. Rep.* **2017**, *7*, 322.
[54] H. G. Ji, M. Maruyama, A. S. Aji, S. Okada, K. Matsuda, H. Ago, *Phys. Chem. Chem. Phys.* **2018**, *20*, 29790.
[55] X. S. Chu, A. Yousaf, D. O. Li, A. A. Tang, A. Debnath, D. Ma, A. A. Green, E. J. G. Santos, Q. H. Wang, *Chem. Mater.* **2018**, *30*, 2112.
[56] D. O. Li, M. S. Gilliam, X. S. Chu, A. Yousaf, Y. Guo, A. A. Green, Q. H. Wang, *Mol. Syst. Des. Eng.* **2019**, *4*, 962.
[57] H. Zhang, C. Li, J. Wang, W. Hu, D. W. Zhang, P. Zhou, *Adv. Funct. Mater.* **2018**, *28*, 1805171.
[58] M. Tosun, S. Chuang, H. Fang, A. B. Sachid, M. Hettick, Y. Lin, Y. Zeng, A. Javey, *ACS Nano* **2014**, *8*, 4948.
[59] L. Yu, A. Zubair, E. J. G. Santos, X. Zhang, Y. Lin, Y. Zhang, T. Palacios, *Nano Lett.* **2015**, *15*, 4928.
[60] S. Liu, K. Yuan, X. Xu, R. Yin, D.-Y. Lin, Y. Li, K. Watanabe, T. Taniguchi, Y. Meng, L. Dai, Y. Ye, *Adv. Electron. Mater.* **2018**, *5*, 1800419.
[61] G. V. Resta, Y. Balaji, D. Lin, I. P. Radu, F. Catthoor, P.-E. Gaillardon, G. De Micheli, *ACS Nano* **2018**, *12*, 7039.
[62] H.-M. Li, D. Lee, D. Qu, X. Liu, J. Ryu, A. Seabaugh, W. J. Yoo, *Nat. Commun.* **2015**, *6*, 6564.
[63] Y. Kim, J. Ryu, M. Park, E. S. Kim, J. M. Yoo, J. Park, J. H. Kang, B. H. Hong, *ACS Nano* **2014**, *8*, 868.
[64] Y. Morikawa, K. Iwata, K. Terakura, *Appl. Surf. Sci.* **2001**, *169*, 11.

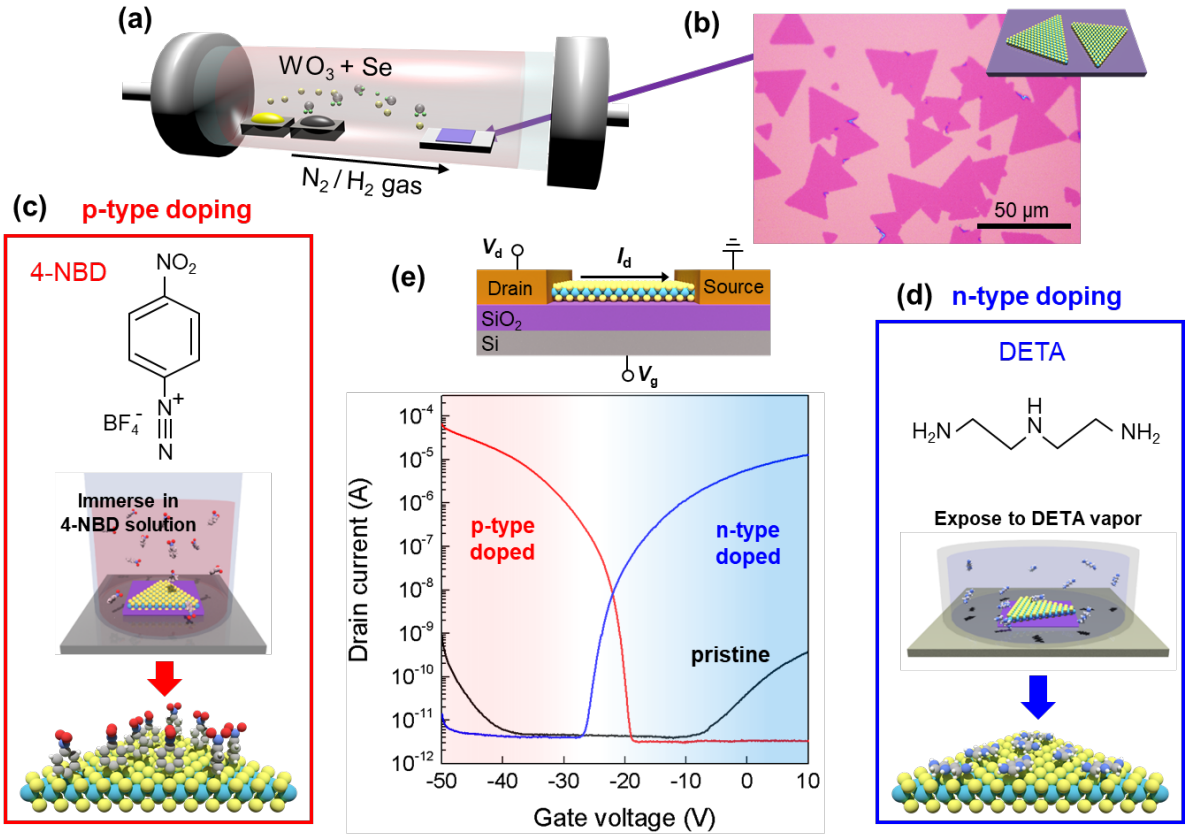

Figure 1. a) Schematic of CVD growth of WSe_2 on SiO_2/Si substrate. b) Optical micrograph of as-grown triangular WSe_2 grains. c,d) Chemical doping processes using 4-NBD and DETA molecules for p- and n-type doping, respectively. e) Transfer characteristics of pristine (black) and 4-NBD doped (red) and DEA doped (blue) WSe_2 devices. The corresponding FET structure is shown in the upper panel of (e). The applied drain voltage (V_d) is 5 V.

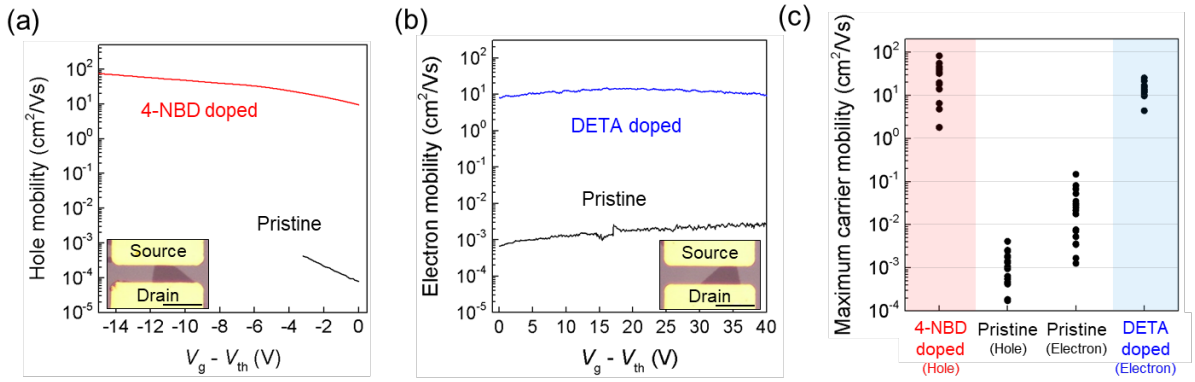

Figure 2. a,b) Effective carrier mobilities of pristine (black) and doped (red and blue) WSe_2 devices plotted as a function of the overdrive gate voltage. Insets show the optical images of the devices (scale bar: 20 μm). c) Distributions of maximum effective hole and electron mobilities of pristine and doped WSe_2.

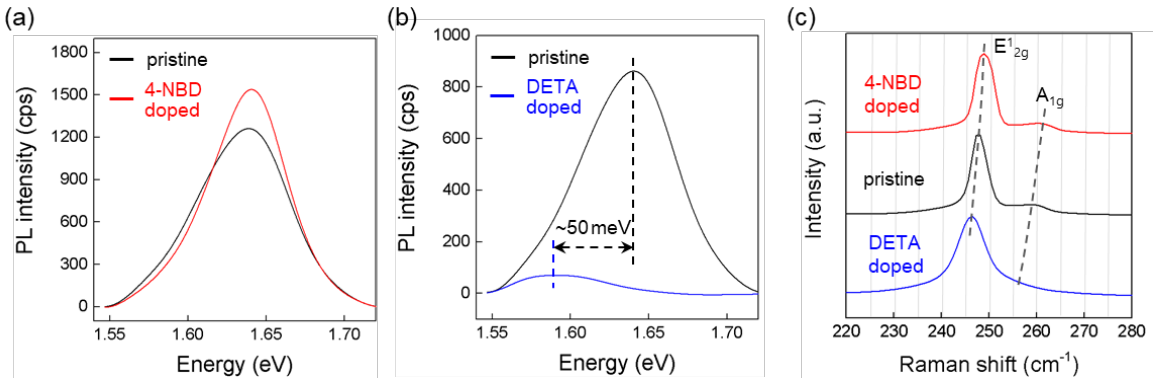

Figure 3. a,b) PL spectra of pristine and doped WSe_2 measured on SiO_2/Si substrates. The identical WS_2 grains were used to monitor the doping-induced spectrum change. c) Raman spectra of pristine and doped WSe_2.

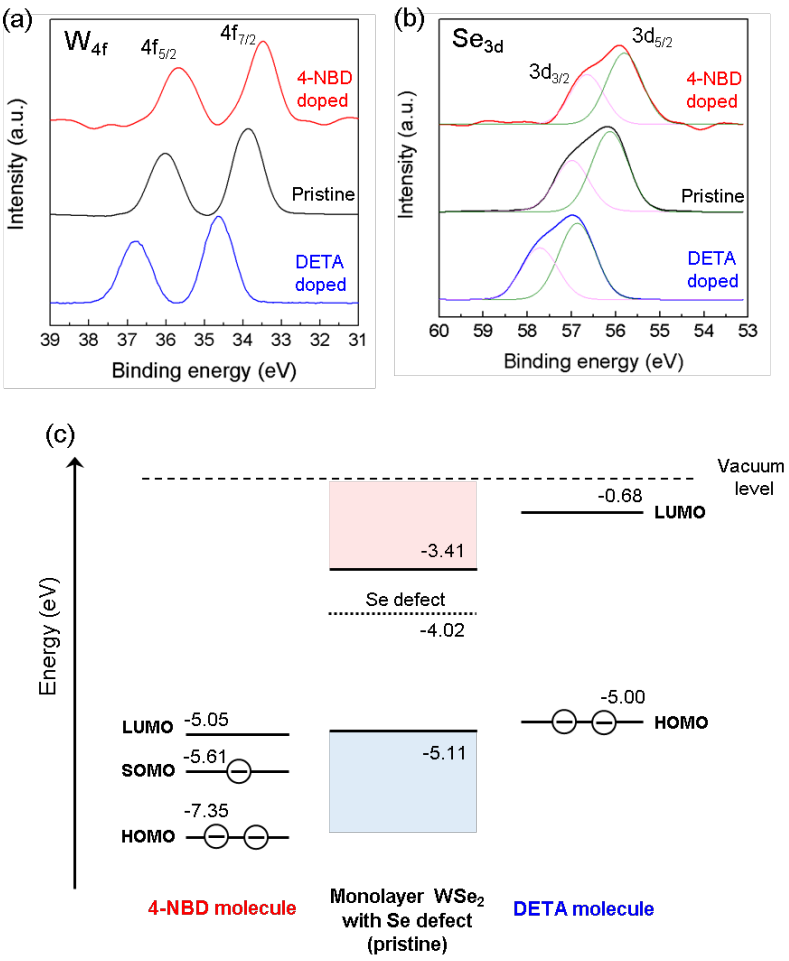

Figure 4. a,b) XPS spectra (W_{4f} and Se_{3d}) of pristine and doped WSe_2. c) Band diagram of pristine WSe_2, 4-NBD and DETA molecules. The band structure of a Se-deficient WSe_2 monolayer is displayed. The energy levels were calculated by DFT.

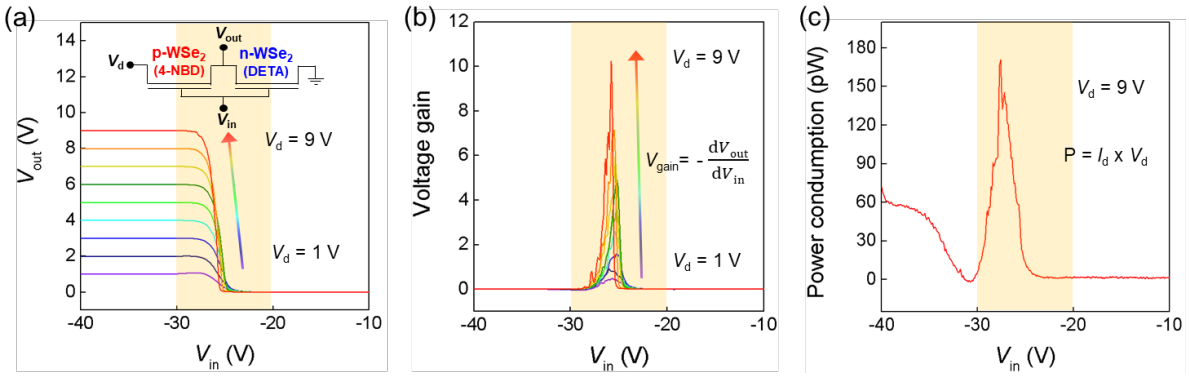

Figure 5. CMOS inverter operated with p- and n-doped WSe_2. a) V_{out} plotted as a function of V_{in}. Inset shows the circuit diagram of the inverter. b,c) Voltage gain and power consumption of the CMOS inverter.

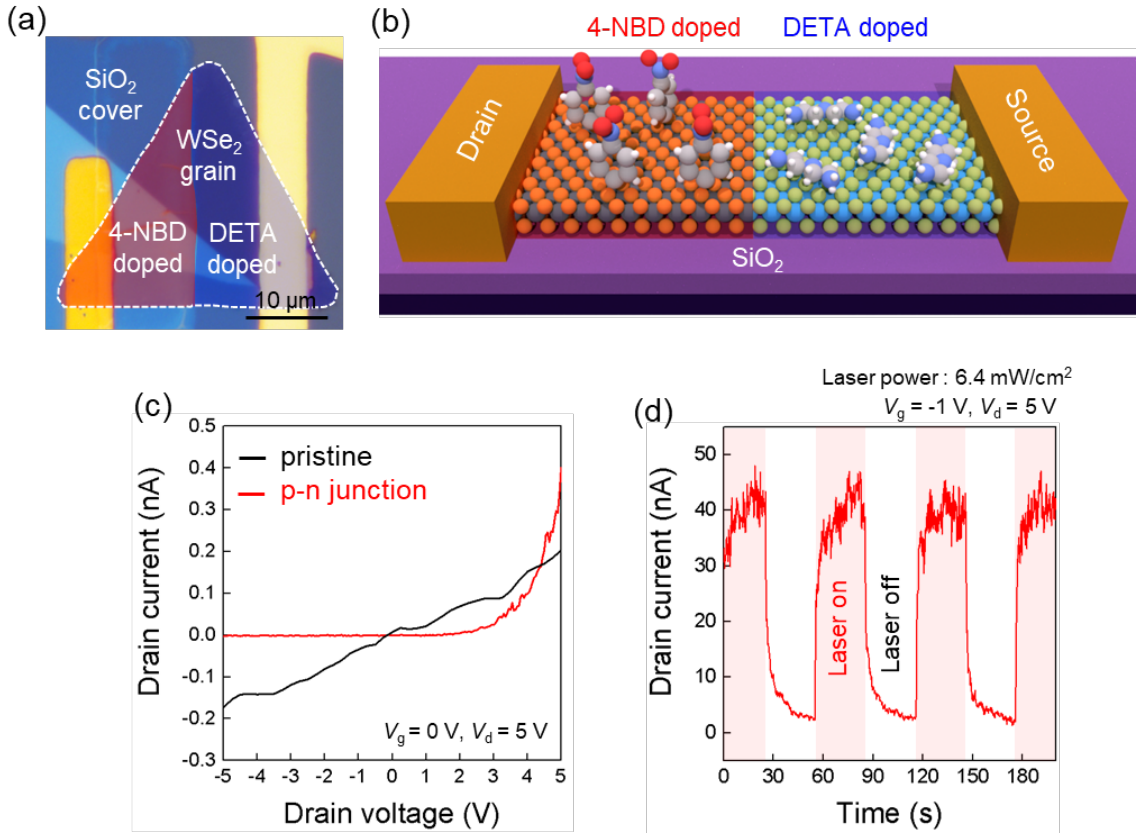

Figure 6. a,b) Optical micrograph and schematic of a p-n junction made by the spatially controlled p/n doping within single WSe_2 grain. c) Output curves of the pristine and p/n doped WSe_2 monolayer device. The device with p-n junction shows clear rectification behavior. d) Light response of the WSe_2 device with p-n junction.

ToC figure

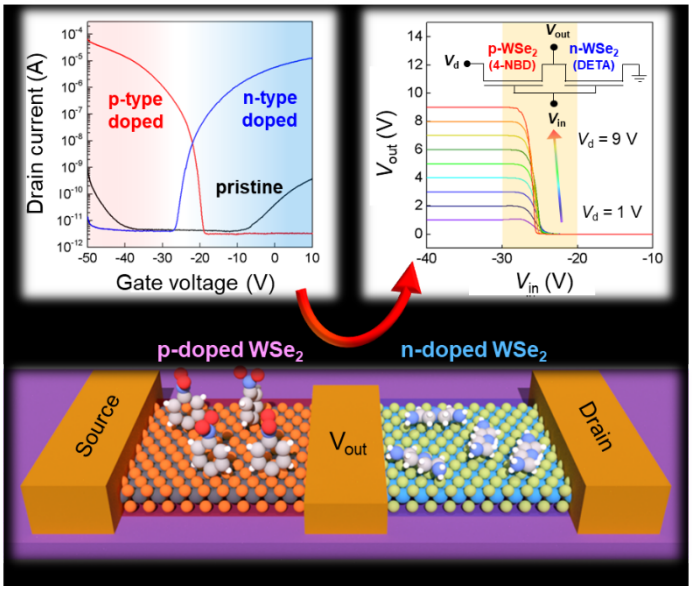
Drain current (A)
Gate voltage (V)
p-type doped
n-type doped
pristine
V_{out} (V)
V_{in} (V)
V_{out}
V_d
p-WSe$_2$ (4-NBD)
n-WSe$_2$ (DETA)
V_{in}
V_d = 9 V
V_d = 1 V
p-doped WSe$_2$
n-doped WSe$_2$
Source
V_{out}
Drain